Phenomenon of ignition and explosion of high-entropy alloys of systems Ti-Zr-Hf-Ni-Cu, Ti-Zr-Hf-Ni-Cu-Co under quasi-static compression

Sergiy Kotrechko, Oleksandra Zatsarna, Oleksandr Filatov, Vadim Bondarchuk, Georgiy Firstov
Kurdyumov Institute for Metal Physics of the National Academy of Sciences of Ukraine, 36 Vernadsky blvd., 03680 Kiev, Ukraine
serkotr@gmail.com, https://orcid.org/0000-0001-5210-4934
alexsandra.ku@gmail.com, https://orcid.org/0000-0003-3200-7672
filatov@imp.kiev.ua, https://orcid.org/0000-0003-1691-4280
vbondar@imp.kiev.ua, https://orcid.org/0000-0003-0931-6231
yuri.firstov@gmail.com, https://orcid.org/0000-0001-7653-9166

Vladimir Dubinko
NSC Kharkov Institute of Physics and Technology, Akademicheskaya Str. 1, Kharkov 61108, Ukraine
vdubinko@hotmail.com, https://orcid.org/0000-0002-6786-7069

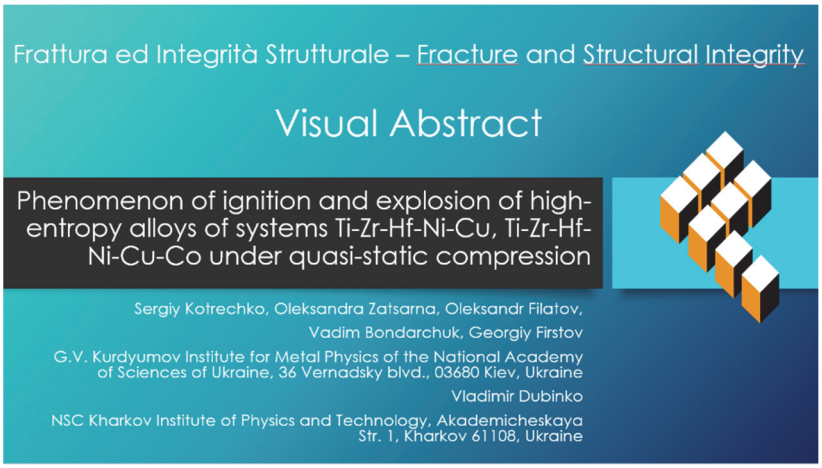

KEYWORDS. Explosive failure, High-entropy alloys, Quasi-static compression, Shear crack, Ignition temperature.

Citation: Kotrechko, S., Zatsarna, O., Filatov, O., Bondarchuk, V., Firstov, G., Dubinko, V., Phenomenon of ignition and explosion of high-entropy alloys of systems Ti-Zr-Hf-Ni-Cu, Ti-Zr-Hf-Ni-Cu-Co under quasi-static compression, Frattura ed Integrità Strutturale, 68 (2024) 410-421.

Received: 31.01.2024
Accepted: 15.03.2024
Published: 22.03.2024
Issue: 04.2024

Copyright: © 2024 This is an open access article under the terms of the CC-BY 4.0, which permits unrestricted use, distribution, and reproduction in any medium, provided the original author and source are credited.

INTRODUCTION

Recently, high-entropy alloys (HEAs) became an active area of the metal research. To date, significant data on the structure and properties of these alloys are accumulated [1, 2]. On the whole, there are two broad classes of HEAs, namely, having fcc and bcc lattices. A characteristic feature of bcc high-entropy alloys is their high strength (hardness), which, in many cases, is combined with sufficient ductility. Besides, most of them are refractory alloys [1, 3-5].

These properties delineate the area of their use as promising structural materials. Ti, Zr, Hf, and Ta are typical elements of refractory high-entropy alloys. At the same time, a new class of functional alloys can be created on the basis of HEAs, namely, high-entropy shape memory alloys [6]. This class of alloys is based on the Ti-Zr-Hf-Ni-Cu and Ti-Zr-Hf-Co-Ni-Cu systems. These compositions are characterized by a high resistance to dislocation movement and by a low diffusion coefficient. This greatly improves the operational characteristics of the functional elements made of these HEAs, in particular, their lifetime.

It is interesting that Ti, Zr and Hf are also considered as the base elements of a whole class of energetic high-entropy alloys due to their outstanding energy release characteristics [7, 8]. A paradoxical situation arises in that bcc-high-entropy alloys of similar chemical composition may be not only structural and functional materials, but can also act as high-energy materials that are designed for the explosive release of thermal energy upon failure.

In this paper, the phenomenon of explosive failure of high-entropy shape memory alloys of the systems Ti-Zr-Hf-Ni-Cu, Ti-Zr-Hf-Co-Ni-Cu under quasi-static compression is ascertained. A model of this phenomenon is suggested. It is shown that ignition and failure by explosion are caused by the release of energy from the oxidation reaction. This reaction is initiated by heating the fine alloy particles due to the heat released ahead of the shear crack tip during the alloy brittle fracture. It is ascertained that this phenomenon is realised when certain critical levels of *strength and ductility* of these alloys are reached. Thus, a boundary is ascertained separating structural and functional high-entropy alloys from high-energy ones.

MATERIALS AND METHODS

The Ti-Zr-Hf-Ni-Cu, Ti-Zr-Hf-Co-Ni-Cu alloys used in the present investigation were arc-melted from iodide Ti, Zr, and Hf, electrolytic Co, Ni, and Cu of high purity in pre-gettered argon. Ingots were turned and re-melted 9 times to ensure adequate homogeneity. The weight of the ingots was typically about 30 g. Scanning electron microscopy studies were carried out using a Zeiss SUPRA 55 VP field emitter scanning electron microscope (FE-SEM) with a lateral resolution 1.2 nm. For the element analysis an EDX system Quantax (silicon drift detector SDD, Series 5010, Type 1108, 30mm², Collimator Zr on Chip, Aperture 3.5mm) from Bruker with the energy resolution of < 125 eV FWHM at MnK (Peakshift 5-300 kcps < 5 eV, at 60 kcps shaper, throughput 1.0 μs shaping time, 100 kcps input count rate) was employed. The crystal structure of the samples was analyzed by X-ray powder diffraction (XRD), using the Bruker AXS D8 Advance diffractometer with θ-2θ Bragg-Brentano geometry and monochromatized Cu Kα1 radiation (λ=1.5406 Å). MAUD software [https://luttero.github.io/maud/] was used for Rietveld refinement. The value of heat capacity was detected with the help of DSC (Netzsch 404 F1) and Proteus software. Elastic modulus at room temperature was measured using instrumented indentation test for hardness (ISO 14577-1:2002(E)) with the help of a "Micron-Gamma" device equipped with Berkovich indenter.

The density of the alloy specimens was measured by hydrostatic weighing. After weighing in both air and water, the density was calculated using the formula:

$$\rho = \frac{\left(P_{\text{air}} \cdot \rho_{\text{liquid}} - P_{\text{liquid}} \cdot \rho_{\text{air}}\right)}{\left(P_{\text{air}} - P_{\text{liquid}}\right)} \tag{1}$$

where P_{air} is the weigh in the air, ρ_{liquid} is the liquid density, P_{liquid} is the weigh in the liquid, ρ_{air} is the air density. The error in determining the density is 0.5%.

The chemical composition, and physical and mechanical properties of the studied alloys are given in Tabs. 1, 2 and 3.

Alloy	Ti	Zr	Hf	Co	Ni	Cu
HEA12	18.15	18.75	14.33	0	21.64	27.13
HEA52	16.67	16.67	16.67	5	20	25
HEA55	16.67	16.67	16.67	10	20	20
HEA56	16.67	16.67	16.67	10	25	15

Table 1: Chemical composition (at. %).

Fractographic investigations and local chemical analysis of the specimens after testing were carried out at an SEM VEGA 3 (TESCAN) equipped with EDX detector XFlash 610M (Bruker). The accelerating voltage was 20kV.
High-speed video shooting took place with a GoPro-4p camera at a frequency of 240 frames per second. The resulting video in the Avidemux video editor was decomposed into separate frames. The duration of each frame was 4.2 ms.

Alloy	Density, kg/m^3	Heat capacity, J/(g, K)	Phase	X-ray density, kg/m^3	Lattice parameters a	b	c	Volume per atom, V/at, Å^3
					Å			
HEA12	8.44	0.253	B2	8.54	3.162	-	-	15.811
			B19`	8.22	3.138	4.1826	5.1164	16.424
HEA52	8.39	0.295	B2	8.86	3.152	-	-	15.653
			B19`	8.58	3.130	4.317	4.853	16.167
HEA55	8.34	0.252	B2	8.57	3.161	-	-	16.126
			B19`	8.75	3.179	4.254	4.845	15.799
HEA56	8.36	0.392	B2	8.79	3.154	-	-	15.686
			B19`	8.81	3.106	4.180	4.938	15.646

Table 2: Atomic structure and physical properties.

Alloy	Specimen diameter d_0, mm	Specimen height h_0, mm	Young's Modulus E, GPa	Yield stress σ_Y^{St}, MPa	Fracture stress σ_f, MPa	Effective value of the yield stress σ_{Yef}, MPa	Plastic strain e_f, %
HEA55-1*	4.03	5.95	75.5	1250	2039	1645	1.57
HEA 55-2*	4.04	6.02	75.5	1250	1881	1500	0.96
HEA 12	4.13	5.63	72.6	1269	2040	1655	4.20
HEA 52	2.96	4.50	69.3	1784	2112	1948	1.80
HEA 56	4.02	5.52	70.7	1657	1904	1781	1.13

* HEA55-1and HEA55-2 - specimens number 1 and 2 from the HEA55 alloy.

Table 3: Mechanical properties.

MECHANICAL TESTING

Cylindrical specimens were used for uniaxial compression tests (Fig. 1). These specimens were made on a lathe, followed by surface grinding.
The roughness of the end surfaces did not exceed 0.63 μm. Specimen sizes are shown in Tab. 3. Tests were performed on an Instron 8802 Universal Servo-Hydraulic Machine at room temperature. The loading rate was 0.05 mm/min. Based on the test results material deformation curves were plotted in the "stress-strain" coordinates (Fig. 2).

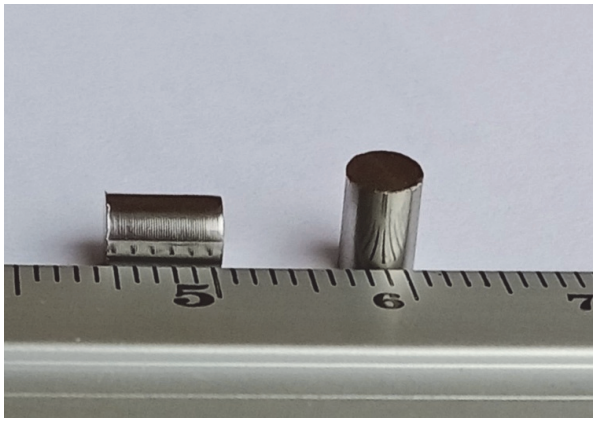

Figure 1: Specimens for uniaxial compression.

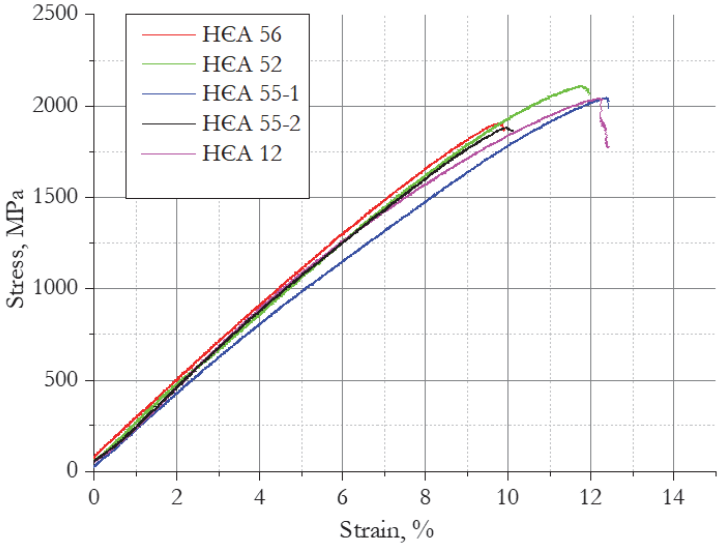

Figure 2: Deformation curves of HEA.

The stress was calculated as:

$$\sigma = F / S_0 \tag{2}$$

where F is the force, S_0 is the cross-sectional area of specimen in the initial (undeformed) state. Compressive strain was calculated as:

$$e = \Delta h / h_0 \tag{3}$$

where Δh is the reduction in the specimen height, h_0 is the initial specimen height.
The use of conditional stresses (dependence (2)) and engineering deformations (dependence (3)) is due to the fact that the maximum strain of specimens didn't exceed 13%. Accordingly, the value of conditional yield strength was calculated as:

$$\sigma_Y^{Sf} = F_{0.2} / S_0 \tag{4}$$

where $F_{0.2}$ is the force at the residual strain $e = 0.2\%$.
Under compression, when the maximum force is reached, failure of the specimen begins, therefore, the compressive strength of material was determined as:

$$\sigma_f = F_{\max} / S_0 \tag{5}$$

where $F_{\max}$ is the maximum value of force on deformation curve.
The corresponding residual strain value was applied as a measure of the plasticity of material under uniaxial compression.

RESULTS AND DISCUSSION

The main stages of failure process

Tab. 3 shows the values of strength and ductility of studied alloys. According to these data, the strength of alloys lies within the range of 1881–2112 GPa. The value of plastic strain varied from 0.96 to 4.20 %. The obtained strengths exceed the typical values for HEAs with a bcc lattice. In particular, for the Ti-Zr-Hf-Ta-Nb alloy, which has a similar chemical composition [1]. However, the investigated alloys have a low ductility, which is because these are cast alloys without thermomechanical treatment. At the same time, a remarkable feature of the studied Ti-Zr-Hf-Ni-Cu and Ti-Zr-Hf-Co-Ni-

Cu alloys is the explosive nature of their failure. Besides, light and sound effects were observed, as well as the flying of hot metal particles that burned in the air (Fig. 3).

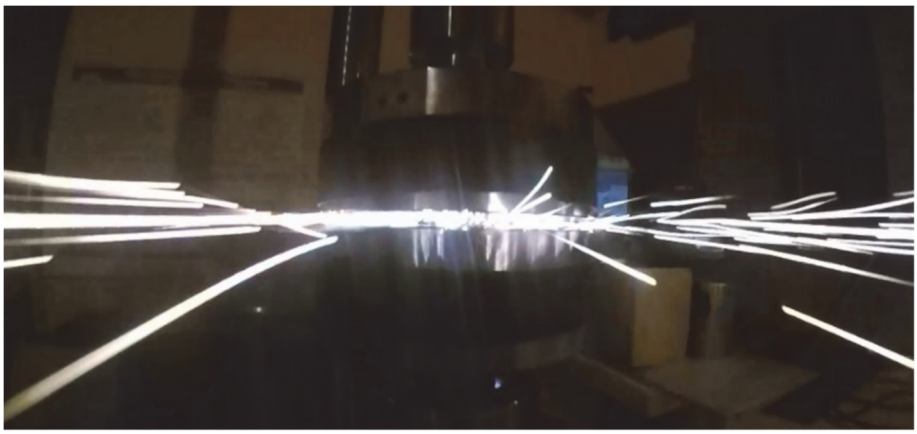

Figure 3: Explosion of HEA55 specimen and ignition of its particles (high-speed shooting, 240 fps).

Analysis showed that the failure process may be divided into three stages:
• The first stage is associated with the initiation of brittle fracture after slight plastic deformation of the specimen.
• The second stage is mechanical instability and the failure of specimen as a result of macroscopic shear realisation.
• At the third stage, flashes were recorded with the flying of burning metal particles.
The morphology of fracture surfaces indicates a brittle fracture initiation mechanism (Fig. 4a). In accordance with classical concepts, at small (~1.0% - 4.0%) plastic deformation in bcc metals and alloys, unstable crack nuclei are formed, the catastrophic growth of which gives rise to brittle fracture at meso- and macroscopic scales. Incompatibility of microscopic deformations at grain or interfacial boundaries is the reason for the crack nuclei formation. It is usually realised due to the dislocation pile-ups (DP) formation. In general case, the crack nuclei (CN) can propagate both in planes normal to the DP plane and directly in this plane [9, 10]. At uniaxial compression, the CNs that opened in the DP plane can grow at meso- and macroscopic scales as transverse shear cracks (Mode II). The fractography of the shear surface is shown in Fig. 4b. The shear occurs at an angle close to 45^0 (Fig. 5).

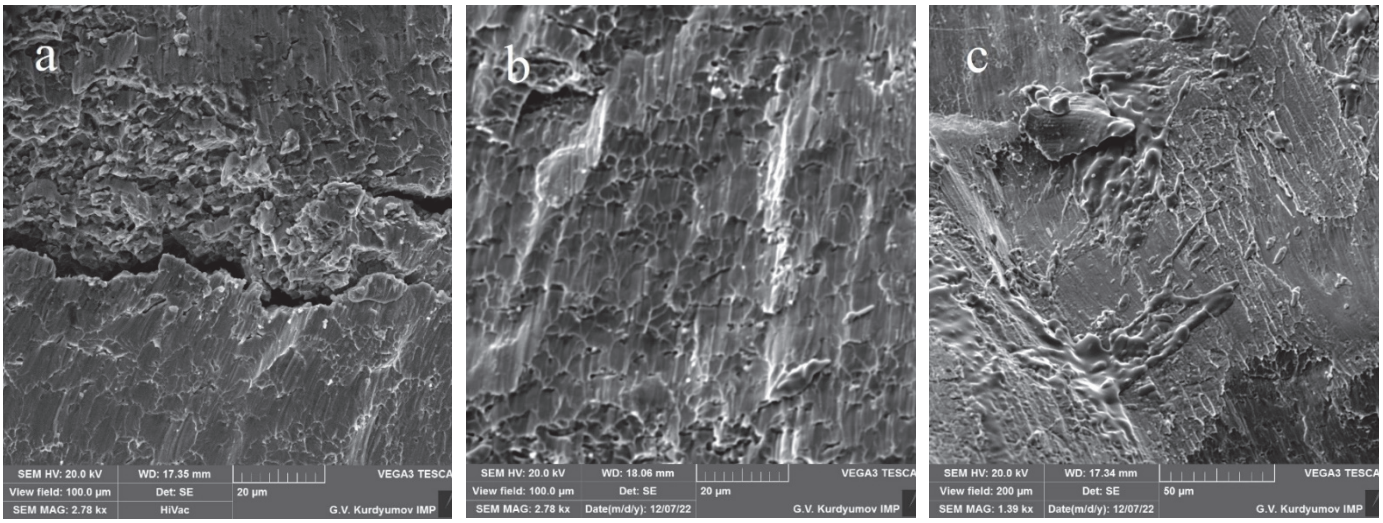

Figure 4: Fractography of the fracture surface (HEA 55): a – brittle fracture surface, b –shear plane surface, c – melting of metal on the fracture surface.

Specific feature of brittle fracture of bcc metals and alloys is that it is initiated by those CNs that become unstable at the moment of their formation [11, 12]. This is one of the reasons why the energy consumption for failure of the crystal lattice at the tip of such submicroscopic CN is insignificant and comparable with the surface energy of metal. At brittle fracture of bcc metals and alloys, this results in the fact that the intensity of release of the accumulated energy of elastic deformations

is much higher than those of energy consumption for failure of metal at the CN tip. This implies an avalanche CNs growth. When a crack propagates at the macroscopic scale, the main part of released energy is spent for the work of local plastic deformation ahead of the crack tip, and, accordingly, for heating the metal in this local region. Thus, at *the first stage of failure*, the CN formation and catastrophic growth at the microscopic scale occur. This results in a shear crack formation. Besides, the metal cracking is observed (Fig. 4a).

Figure 5: Specimen before and after failure (HEA52).

The second stage consists in the accelerated propagation of a shear crack at the meso- and macroscopic scales. The start of the third stage of failure should be considered the heating of microparticles formed as a result of metal cracking in a local area near the crack tip to a critical temperature at which the oxidation reaction begins. According to the obtained experimental data, the release of energy of the chemical reaction of oxidation leads to the ejection of small metal particles and their ignition (Fig. 3). Part of this energy is spent for melting metal on the shear surface (Fig. 4c). It is known that small particles of Zr and its alloys can ignite in the air at sufficiently low temperatures. Thus, the ability to ignite ZrW alloy particles, which size doesn't exceed 100–200 μm, was experimentally shown [13]. These particles were formed by brittle fracture of the ZrW alloy under dynamic loading using a split Hopkinson pressure bar. According to [13], heating up to several hundred degrees is quite sufficient for the ignition of small particles of the studied ZrW alloy. In our case, the key importance for the ignition of HEA under quasi-static uniaxial compression is the possibility of reaching this critical temperature to start the oxidation reaction. It is due to heating metal ahead of the shear crack tip during its dynamic propagation at brittle fracture of specimen. Therefore, the crack front plays the role of a linear energy source that propagates in the shear plane and triggers the oxidation process. So, friction of the shear crack planes, which are pressed with a force $\sigma_f S_{con}/2$ (S_{cont} is the contact area of the crack planes) provides additional grinding of metal and formation of small particles. The scattering trajectories of the smallest particles are visualised as flashes (Fig.6a). Larger particles explode in the flight (Fig. 6b). This agrees well with the kinetics of ignition and combustion of ZrW alloy particles, which was studied in [13,14]. The only difference was that in these works, a dynamic load was used to grind the alloy and heat it.

Estimation of the value of metal heating temperature at the crack shear tip

To estimate roughly the heating temperature of metal ahead of the crack tip, it suffices to consider the corresponding problem in the adiabatic approximation for a stationary crack of the Mode II. According to the classical concepts, the amount of released energy of elastic deformation during the formation of a crack with a half-length l_f is defined as:

$$W = \frac{\pi\beta}{E}\tau_f^2 l_f^2 \tag{6}$$

where W is the "elastic' energy per unit specimen thickness; τ_f is the applied shear macrostress; E is the Young modulus; for the plane strain $\beta = 1 - \nu^2$; ν is the Poisson's ratio.
This energy is spent on the formation of new surfaces and the work of plastic deformation in the vicinity of the crack tip:

$$\frac{\pi\beta}{E}\tau_f^2 l_f^2 = 4\gamma l_f + A_Y \tag{7}$$

where γ is the specific energy of failure, which, in the first approximation, is equal to the specific surface energy; A_Y is the work of local plastic deformation per unit thickness of the specimen.

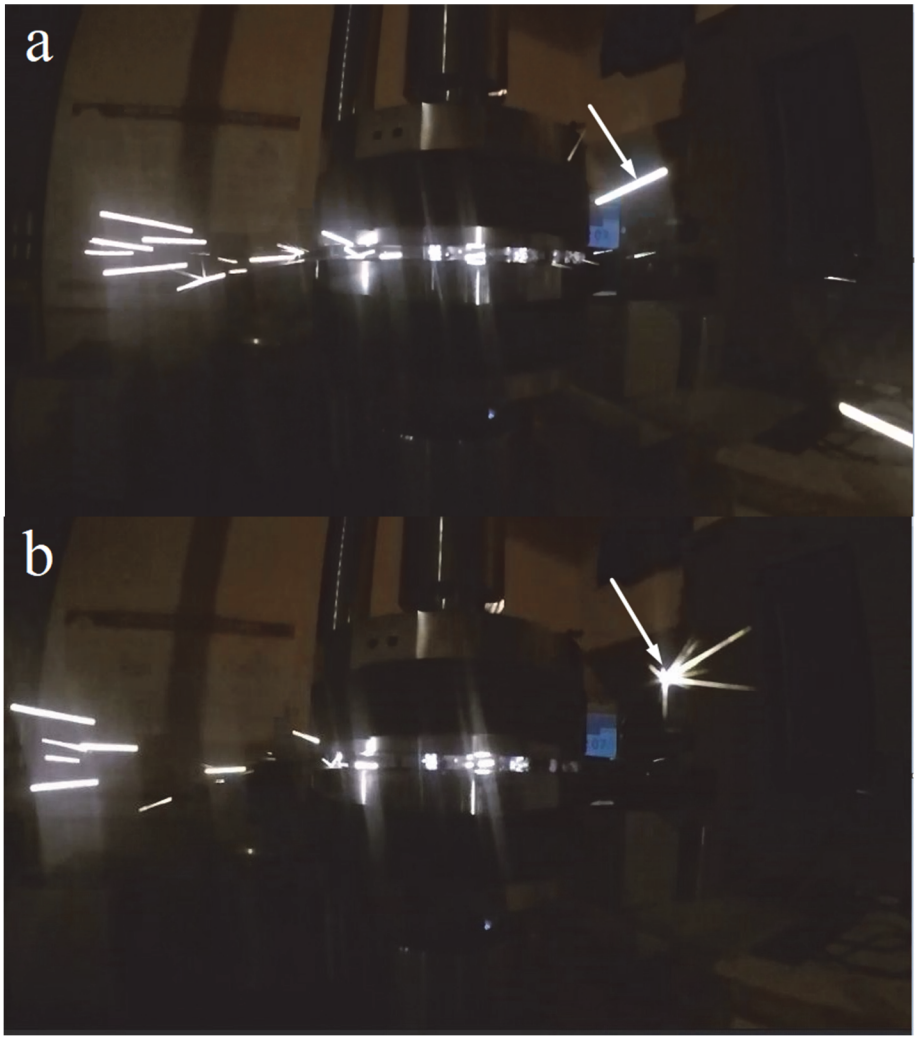

Figure 6: Flying of burning particles. The arrow shows a large particle (a) that ignites during flight (b). (Sample HEA55, shutter speed 0.004 s., shooting speed 240 fps).

In the adiabatic approximation, it is usually assumed that almost all of this work is spent for heating metal in the local yield region, i.e.:

$$\eta A_Y = C\rho S_Y \Delta T_Y \tag{8}$$

where ΔT_Y is the average value of the metal temperature increase within the local yield region; ρ and C are the density and specific heat capacity of metal, respectively; S_Y is the area of local yield region; for metals $\eta \approx 0,9$ [13].

For a transverse shear crack in the first approximation (see Appendix A):

$$S_Y \approx \frac{\pi \cdot \left[3.75 + \left(1 - 2\nu^2\right)\right]}{4} \cdot \left(\frac{\tau_f}{\sigma_Y}\right)^4 \cdot l_f^2 \tag{9}$$

Substituting (9) to (8) and taking into account (6) and (7):

$$\Delta T \approx \frac{4\eta\left(\frac{\pi\beta}{E} \cdot \tau_f^2 l_f - 4\gamma\right)}{\pi \cdot C\rho\left[3.75 + \left(1 - 2\nu^2\right)\right] \cdot \left(\frac{\tau_f}{\sigma_Y}\right)^4 \cdot l_f} \tag{10}$$

In our case (see Appendix B):

$$\frac{\pi\beta}{E}\tau_f^2 l_f >> 4\gamma \tag{11}$$

whence

$$\Delta T_Y \approx \frac{4\eta\beta\tau_f^2}{C\rho E \left[3.75 + \left(1 - 2\nu^2\right)\right] \cdot \left(\frac{\tau_f}{\sigma_Y}\right)^4} \tag{12}$$

Note that σ_Y is the yield strength of metal at strain rate ahead of dynamic crack tip. For bcc metals and alloys, this value can significantly exceed the value σ_Y^{st} under quasi-static load. The data given in [13, 15,16] enable to estimate σ_Y:

$$\sigma_Y \approx \left(1.5 \div 2\right) \sigma_Y^{st} \tag{13}$$

In our case, the critical stress applied to the transversal shear crack, τ_f, can be estimated as:

$$\tau_f = \frac{1-\mu}{2}\sigma_f \tag{14}$$

where σ_f is the macroscopic fracture stress of a specimen; $\mu \approx 0.3$ is the friction coefficient [17].

This dependence takes into account the fact that the sides of a shear crack are pressed against each other by a force of $\sigma_f/2$. At $\sigma_f \approx 2000\text{MPa}$ and $\mu \approx 0.3$ one has $\tau_f \approx 700 MPa$.

Dependence (9) for the area of local yield region and, accordingly, relation (12) for the increase in the average temperature in this region, are obtained in the approximation of an ideally plastic material. It means that the effect of strain hardening isn't taken into account. This is due to the fact that above effect, when determining the sizes of local yield region ahead of a crack, considerably complicates the problem and requires to employ numerical methods. So, the effective value is usually applied to estimate the yield stress σ_{Yef}^{st}. According to [18], in our case:

$$\sigma_{Yef}^{st} = \frac{\sigma_Y^{st} + \sigma_f}{2} \tag{15}$$

At $\sigma_Y^{st} \approx 1000\text{MPa}$ and $\sigma_f \approx 2000\text{MPa}$ one has $\sigma_{Yef}^{st} \approx 1500\text{MPa}$. Calculations with account of (13), give $\sigma_Y^{st} \approx 2250 \div 3000\text{MPa}$.

Substituting these values into (12), and accounting for the mean values (Tabs. 2, 3) for $C = 298\ J/kgK$, $\rho = 8480\ kg/m^3$ and $E = 72GPa$; at $\eta = 0,9$ and $\nu = 0,3$, gives $\Delta T_Y \approx 209 \div 690K$. Such an increase in the local temperature is quite sufficient to initiate an oxidation reaction of Zr-rich particles. These values agree well with the data given in [13].

The main factors inducing explosive failure of HEA

The results obtained make it possible the main factors leading to ignition and explosive failure of both the investigated HEA alloys and Ti-Zr-Hf -based HEA in general, namely:

- Brittle mechanism of the alloy fracture initiation.
- High level of brittleness of the alloy (low ductility).
- High absolute yield strength of the alloy (high hardness).

The brittle nature of fracture plays a key role among these factors, since it ensures low energy consumption for fracture, as a result of which almost all the energy released during crack growth is spent for local heating of metal ahead of the crack tip. At the initial stages of crack growth, a great difference between the amount of released energy and the energy consumption for its growth is the cause of crack acceleration, that is, the reason for its dynamic growth from micro- to macro-sizes, which is a necessary condition for increasing the temperature at its tip. As is known, crack growth during brittle fracture of bcc metals and alloys is realised due to the "counter-cleavage" mechanism, that is, by the CN formation in the "process zone" at the tip of the main crack and their counter-growth [11]. Together with the friction of the crack planes, this provides grinding of the material into small particles, for the ignition of which quite low (of the order of hundreds of degrees) temperature increase is sufficient. In contrast, with a ductile mechanism of metal fracture at the crack tip, it grows relatively slowly, which increases the time for heat removal and, accordingly, reduces the temperature increase at its tip. Besides, during the ductile crack growth, there is no metal cracking, which is necessary to obtain fine metal particles. Thus, transition from brittle to ductile fracture is one of the effective ways to prevent ignition and explosive fracture. In certain situations, this can be achieved by specimens heating. At the first glance, this sounds paradoxical, but it is possible to explain why, in [15], specimens made of the Ta-Nb-Hf-Zn-Ti alloy failed without ignition under impact loads even at a temperature of 873 K. Moreover, it was shown in [7] that even under impact loading, transition of Ti-Zn-Hf-$X_{0.5}$ alloys from ductile to brittle fracture with *decreasing specimen temperature* "made the crack tip more prone to production of hots spots and induced strong impact ignition reaction".

The brittle nature of fracture is a *necessary* condition for ignition of specimens under quasi-static compression. In this case, the value of heating temperature of metal at the crack tip depends significantly on both the absolute value of yield strength σ_{Yef}^{st} and the ratio $\sigma_{Yef}^{st} / \sigma_f$. Really, substituting expression (14) into (12) and writing the relationship between σ_Y and σ_{Yef}^{st} as:

$$\sigma_Y = \alpha \sigma_{Yef}^{st} \tag{16}$$

where α is the coefficient:

$$\Delta T_Y = \frac{4\eta\beta\alpha^4}{C\rho E\left[3.75 + \left(1-2\nu^2\right)\left(1-\mu\right)^2\right]} \times \left(\frac{\sigma_{Yef}^{st}}{\sigma_f}\right)^2 \times \left(\sigma_{Yef}^{st}\right)^2 \tag{17}$$

Ratio $\sigma_{Yef}^{st} / \sigma_f$ characterises the metal brittleness. Its maximum value $\sigma_{Yef}^{st} / \sigma_f = 1$. For investigated alloys $\sigma_{Yef}^{st} / \sigma_f \approx 0.5 - 0.9$. Besides, for ignition, the material must have a sufficiently high *absolute* value of σ_{Yef}^{st} $\left(\sigma_{Yef}^{st} \geq 1000\text{MPa}\right)$, i.e., it must be sufficiently hard.

The physical meaning of these factors effect on ΔT_Y is that they govern the area of local yield region ahead of the crack tip. According to (9) and (14), the higher is the ratio $\sigma_{Yef}^{st} / \sigma_f$ and the absolute value of σ_{Yef}^{st}, the lower is the area of local

yielding region. At a fixed value of the released energy, a decrease in the area of heat release region gives rise to an increase in the thermal energy concentration, and, respectively, to an increase in local temperature in this region.

Thus, avoidance the brittle fracture mechanism is a key factor in the prevention of ignition of Ti-Zr-Hf-Cu and Ti-Zr-Hf-Co-Ni-Cu HEAs under quasi-static compression. This is especially urgent for high effective yield strengths $\sigma_{Yef}^{st} \geq 1000 MPa$ and high brittleness of the alloy $\sigma_{Yef}^{st} / \sigma_f \geq 0,5-0,9$. As the first approximation, the obtained values of σ_{Yef}^{st} and $\sigma_{Yef}^{st} / \sigma_f$ can be considered as critical. These conclusions are confirmed by the data of [8], in which the effect of explosive failure at uniaxial compression was found for HEAs Ti-Zr-Hf-$Al_{0.3}$, Ti-Zr-Hf-$Cu_{0.3}$, Ti-Zr-Hf-$Ni_{0.3}$. Processing of the data given in this work shows that for these alloys $\sigma_{Yef}^{st} = 1010 \div 1029 \text{MPa}$, and the value of brittleness parameter $\sigma_{Yef}^{st} / \sigma_f \geq 0,85-0,91$. This agrees well with the ascertained critical values of strength and brittleness parameter.

In general, the high strength of HEAs containing Ti-Zr-Hf makes them promising *structural* and *functional* materials having advantages over existing alloys. However, when critical levels of strength and brittleness are reached, these alloys demonstrate "opposite" properties turning into *high-energetic* alloys, i.e. capable of explosive release of a significant amount of thermal energy. In fact, the ascertained critical values of strength and brittleness "delineate" the boundary separating structural and functional high-entropy alloys from energetic high-entropy alloys. This is an important feature of this class of high-entropy alloys, which must be taken into account when searching for their optimal mechanical properties and compositions.

CONCLUSIONS

1. High-entropy alloys containing Ti-Zr-Hf, in particular, alloys of the Ti-Zr-Hf-Ni-Cu and Ti-Zr-Hf-Co-Ni-Cu systems are prone to explosive fracture with ignition under quasi-static compression. The reason for this phenomenon is the energy release of the alloy oxidation reaction, which is initiated due to the heat released ahead of the shear crack, which is formed at brittle fracture of specimen under quasi-static compression.
2. Failure of the investigated alloys at quasi-static compression occurs in three stages:
– initiation of brittle fracture after small (1% ÷ 4%) plastic strains;
– formation of a dynamic shear crack;
– initiation of an oxidation reaction, ignition and explosive failure of a specimen.
3. Brittle mechanism of the alloy failure is a necessary condition for ignition and explosion. A sufficient condition is high effective yield strength $\sigma_{Yef}^{st} \geq 1000 MPa$ and high brittleness of the alloy (the ratio of the effective yield stress σ_{Yef}^{st} to the fracture stress σ_f must be higher than 0.5). This value σ_{Yef}^{st} and the ratio $\sigma_{Yef}^{st} / \sigma_f$ may be considered as the lower estimation of the boundary of transition of structural and functional high-entropy alloys containing Ti-Zr-Hf into energetic high-entropy alloys.

ACKNOWLEDGEMENTS

The research leading to these results was funded by the National Academy of Sciences of Ukraine (Grant number 0121U107569)

REFERENCES

[1] George, O. E., Raabe, D., Ritchie, R. O. (2019). High- entropy alloys, Nat. Rev. Mater., 4, pp. 515-534. DOI: 10.1038/s41578-019-0121-4
[2] Tsai, M.-H. (2016). Three Strategies for the Design of Advanced High-Entropy Alloys, Entropy, 18, 252. DOI: 10.3390/e18070252.
[3] Moravcikova-Gouvea, L., Moravcik, I., Pouchly, V., Kovacova, Z., Kitzmantel, M., Neubauer, E., Dlouhy, I. (2021). Tailoring a Refractory High Entropy Alloy by Powder Metallurgy process Optimization, Materials, 14.

DOI: 10.3390/ma14195796.
[4] Gao, M. C., Carney, C.S., Dogan O., Jablonski, P. D., Hawk, J. A., Alman, D. E. (2015). Design of refractory high-entropy alloys, JOM, 67, pp. 2653–2669. DOI: 10.1007/s11837-015-1617-z
[5] Dirras, G., Couque, H., Lilensten, L., Heczel, A., Tingaud, D., Couzinié, J.-P., Perrière, L., Gubicza, J., Guillot, I. (2016). Mechanical behavior and microstructure of $Ti_{20}Hf_{20}Zr_{20}Ta_{20}Nb_{20}$ high-entropy alloy loaded under quasi-static and dynamic compression conditions, Mater. Charact., 111, pp. 106–113. DOI: 10.1016/j.matchar.2015.11.018.
[6] Firstov, G. S., Kosorukova, T. A., Koval, Yu N., Verhovlyuk, P. A. (2015). Directions for High-Temperature Shape Memory Alloys' Improvement: Straight Way to High-Entropy Materials? Shape Mem. Superelasticity, 1, pp. 400-407. DOI: 10.1007/s40830-015-0039-7.
[7] Chen, J. Chen, C., Guo, K., Chang, M., Wang, R., Han, Y., Cheng, C., Tang, E. (2023). Dynamic mechanical properties and ignition behavior of TiZrHfX0.5 high- entropy alloys associated with temperature, trace element and strain rate, J. Alloys Compd., 933. DOI: 10.1016/j.jallcom.2022.167798
[8] Chen, C. Guo, Y., Gao, R., Guo, K., Chang, M., Han, Y., He, L., Tang, E. (2022). Influencing mechanism of trace elements on quasi-static ignition of TiZrHf-based high-entropy alloys, Mater. Sci. Technol, 38, pp. 1230–1238. DOI: 10.1080/02670836.2022.2075171
[9] Kotrechko, S., Dnieprenko, V. (2003). Nucleation of micro-cracks for polycrystalline metal with anisotropy: micro-stress evaluation, Theor. Appl. Fract. Mech., 40, pp. 271-277. DOI: 10.1016/j.tafmec.2003.09.002
[10] Knott, J. *F.* (1973). Fundamentals of fracture mechanics, Butterworth&CoPublishersLt; Publicationdate.
[11] Bordet, S., R., Karstensen, A., D., Knowles, D., M., Wiesner, C., S. (2005). A new statistical local criterion for cleavage fracture in steel. Part I: Model presentation, Eng. Fract. Mech., 72, pp. 435–452. DOI: 10.1016/j.engfracmech.2004.02.009
[12] Kotrechko, S., Kozák, V., Zatsarna, O., Zimina, G., Stetsenko, N., Dlouhý, I. (2021). Incorporation of Temperature and Plastic Strain Effects into Local Approach to Fracture, Materials, 14. DOI: 10.3390/ma14206224
[13] Ren, H., Liu, H., Ning, J. (2016). Impact-initiated behavior and reaction mechanism of W/Zr composites with SHPB setu, AIP Advances, 6. DOI: 10.1063/1.4967340
[14] Wei H. and Yoo C. (2012). Kinetics of small single particle combustion of zirconium alloy, J. Appl. Phys., 111. DOI: 10.1063/1.3677789
[15] Hu, M., Song, W., Duan, D., Wu, Y. (2020). Dynamic behavior and microstructure characterization of TaNbHfZrTi high-entropy alloy at a wide range of strain rates and temperatures, Int. J. Mech. Sci., 182. DOI: 10.1016/j.ijmecsci.2020.105738
[16] Zhong, X., Zhang, Q., Ma, M., Xie, J., Wu, M., Ren, S., Yan, Y. (2022). Dynamic compressive properties and microstructural evolution of $Al_{1.19}Co_2CrFeNi_{1.81}$ eutectic high entropy alloy at room and cryogenic temperatures, Mater. Des., 219. DOI: 10.1016/j.matdes.2022.110724
[17] Ashish K. Kasar , Kelsey Scalaro and Pradeep L. Menezes. (2021). Tribological Properties of High-Entropy Alloys under Dry Conditions for a Wide Temperature Range, A Review. Materials, 14. p.5814. DOI: 10.3390/ma14195814
[18] ASTM E1921-21 Standard Test Method for Determination of Reference Temperature, T_0, for Ferritic Steel sin the Transition Range. DOI: 10.1520/E1921-21 ICS Code:77.040.10.
[19] Anderson, T.L. (2017). Fracture Mechanics Fundamentals and Applications, Fourth Edition CRC Press by Taylor & Francis Group.

APPENDIX A: ESTIMATION OF THE AREA OF PLASTIC DEFORMATION REGION AHEAD OF A TRANSVERSE SHEAR CRACK (OF MODE II)

Based on both the stress distribution ahead of a crack tip (of Mode II) and the von Mizes yielding criterion, the first approximation for dependence of the distance from the crack tip to the plastic region boundary, $r_p(\theta)$, can be derived [19]. In polar coordinates at plane strain deformation, it may be written as follows:

$$r_Y(\theta)=\frac{K_{II}^2}{2\pi\sigma_Y^2}\left[3\left(1-\frac{3}{4}\sin^2\theta\right)+\left(1-2\nu^2\right)\sin^2\frac{\theta}{2}\right] \tag{A1}$$

where K_{II} is the stress intensity coefficient; σ_Y is the yield stress; θ is the polar angle; ν is the Poisson's ratio. Accordingly, the expression for the plastic region area is the following:

$$S_Y = \frac{K_{II}^4}{4\pi^2\sigma_Y^4} 2\int_0^{\pi}\left[3\left(1-\frac{3}{4}\sin^2\theta\right)+\left(1-2\nu^2\right)\sin^2\frac{\theta}{2}\right]d\theta \tag{A2}$$

After integration:

$$S_Y = \frac{3.75+\left(1-2\nu^2\right)}{4\pi}\left(\frac{K_{II}}{\sigma_Y}\right)^4 \tag{A3}$$

Taking into account that:

$$K_{II} = \tau_f\sqrt{\pi l_f} \tag{A4}$$

where τ_f is the macroscopic shear stress; l_f is the shear crack half-length.
Substituting (A4) into (A3) gives rise to:

$$S_Y = \frac{\pi\left[3.75+\left(1-2\nu^2\right)\right]}{4}\times\left(\frac{\tau_f}{\sigma_Y}\right)^4 l_f^2 \tag{A5}$$

APPENDIX B: ESTIMATION OF THE CRACK SIZE AT WHICH ENERGY COSTS FOR FRACTURE AT THE CRACK FRONT ARE SIGNIFICANTLY LESS THAN THE COSTS FOR LOCAL PLASTIC DEFORMATION

As noted above, at brittle fracture of bcc metals and alloys, low energy costs for fracture of the crystal structure ahead of the crack nuclei of submicroscopic sizes causes their avalanche growth. The excess of released elastic energy goes to form the local yielding region and to heat it. In the Eqn. (7), this effect is characterized by the difference:

$$\frac{\pi\beta}{E}\tau_f^2 l_f^2 - 4\gamma l_f \tag{B1}$$

This expression enables to estimate the crack length l_f, at which the energy costs for fracture ahead of the crack tip, 4γ, is quite negligible:

$$\frac{\pi\beta}{E}\tau_f^2 l_f >> 4\gamma \tag{B2}$$

where

$$l_f >> \frac{4\gamma E}{\pi\beta\tau_f^2} \tag{B3}$$

Substitution of the upper limit for specific energy of failure, $\gamma = 10 J/m^2$, at $E = 72GPa$, $\tau_f = 0.7GPa$, $\beta = 0.9$, gives rise to the following estimation - $l_f \gg 2\ \mu\text{m}$.
This means that when the crack length approaches to the specimen size ($l_f \geq 2$ mm), the term 4γ in the Eqn. (10) can be neglected, i.e. almost all released energy is spent for plastic deformation ahead of the crack tip.